

CIC: Circular Image Compression

Honggui LI^{1*}, Sinan CHEN², Nahid MD LOKMAN HOSSAIN³, Maria TROCAN⁴, Dimitri GALAYKO⁵,
Mohamad SAWAN^{6,7}

^{1,2,3}School of Information Engineering, Yangzhou University, Yangzhou 225127, China

⁴LISITE Research Laboratory, Institut Sup érieur d'Électronique de Paris, Paris 75006, France

⁵Laboratoire d'Informatique de Paris 6, Sorbonne University, Paris 75020, France

⁶Polystim Neurotech Laboratory, Polytechnique Montreal, Montreal H3T1J4, Canada

⁷School of Engineering, Westlake University, Hangzhou 310024, China

¹hgli@yzu.edu.cn, ²32234352677@qq.com, ³mh23083@stu.yzu.edu.cn, ⁴maria.trocan@isep.fr,

⁵dimitri.galayko@sorbonne-universite.fr, ⁶mohamad.sawan@polymtl.ca, ⁷sawan@westlake.edu.cn

*Corresponding Author

Abstract: Learned image compression (LIC) is currently the cutting-edge method. However, the inherent difference between testing and training images of LIC results in performance degradation to some extent. Especially for out-of-sample, out-of-distribution, or out-of-domain testing images, the performance of LIC dramatically degraded. Classical LIC is a serial image compression (SIC) approach that utilizes an open-loop architecture with serial encoding and decoding units. Nevertheless, according to the theory of automatic control, a closed-loop architecture holds the potential to improve the dynamic and static performance of LIC. Therefore, a circular image compression (CIC) approach with closed-loop encoding and decoding elements is proposed to minimize the gap between testing and training images and upgrade the capability of LIC. The proposed CIC establishes a nonlinear loop equation and proves that steady-state error between reconstructed and original images is close to zero by Taylor series expansion. The proposed CIC method possesses the property of Post-Training and plug-and-play which can be built on any existing advanced SIC methods. Experimental results on five public image compression datasets demonstrate that the proposed CIC outperforms five competing state-of-the-art open-source SIC algorithms in reconstruction capacity. Experimental results further show that the proposed method is suitable for out-of-sample testing images with dark backgrounds, sharp edges, high contrast, grid shapes, or complex patterns.

Keywords: Circular Image Compression, Learned Image Compression, Plug-and-Play, Steady-State Error, Taylor Series Expansion.

I. INTRODUCTION

In the contemporary world of big data and generative artificial intelligence, a large amount of images are produced in various ways moment by moment [1]. Hence, it is necessary to efficiently compress images before transmission, storage,

analysis, processing, recognition, and understanding [2-3]. Image compression methods can be divided into two categories: lossy and lossless image compression [4]. The former seeks for the balance between bitrate and distortion, the latter seeks for minimum bitrate without distortion. Image compression methods can also be partitioned into two categories: model-based and learning-based image compression [5]. The former develops to the full, and the latter is the front research direction and can be named as end-to-end deep learning-based image compression, learning-driven image compression, or learned image compression (LIC).

Because LIC is data-driven, deep neural network is firstly optimized by training image datasets and finally evaluated by testing image datasets. Training and testing image datasets hold similar but not identical characteristics. Deep neural network is optimal for training image datasets and is not always optimal for testing image datasets. Thus, the discrepancy between testing and training image datasets leads to performance degradation to some degree. Particularly for out-of-sample, out-of-distribution, or out-of-domain testing images, the performance of LIC dramatically degrades [6-8]. Hence, it is vitally important to improve the output of trained deep neural network based on testing image datasets to achieve ideal image reconstruction performance.

LIC usually utilizes an open-loop architecture with serial encoding and decoding units and can be named as serial image compression (SIC). Closed-loop architecture is widely adopted in automatic control systems to obtain extraordinary static and dynamic performance. According to the theory of automatic control, closed-loop architecture is superior to open-loop architecture in steady and transient states capability [9-10]. Therefore, circular image compression (CIC) method with closed-loop encoding and decoding elements is proposed to minimize the gap between training and testing image datasets and improve the reconstruction performance of LIC. It is worth mentioning that the proposed method is an extension of our previous work, circular image super-resolution, circular image compressive sensing, and circular compressed image super-resolution [11-13].

The proposed CIC is described by a nonlinear loop equation which is resolved by Taylor series expansion. Taylor series is an efficient tool for nonlinear analysis and has already been used for deep learning and LIC [14-15]. P. X. Wei et al propose a

Taylor neural network with Taylor series approximation [14]. Y. E. Bao et al present a Taylor series expansion of sinusoidal functions based two-branch nonlinear transformation architecture to eliminate correlations from images [15].

In the present realm of large language models, there are many excellent pretrained SIC models which are openly and freely released on the Internet, such as GitHub and HuggingFace. They provides the opportunity to upgrade the performance of the pretrained SIC models in the way of plug-and-play and Post-Training. Actually, plug-and-play policy is widely employed in deep learning-based image restoration including the decoding of lossy image compression [16-21]. The proposed CIC can be built on any existing advanced pretrained SIC models and lift their performance in the form of plug-and-play and Post-Training.

The key innovations of this paper are listed as follows:

- closed-loop CIC framework with encoding and decoding elements;
- plug-and-play and Post-Training attribution established on any leading pretrained SIC models;
- nonlinear loop equation and complete mathematical proof of zero steady-state error with linear approximation of Taylor series expansion;
- huge performance boost in peak signal-to-noise ratio (PSNR), structural similarity (SSIM), and bits per sub pixel (BPSP); absolute and logic difference image blocks which demonstrate the extraordinary reconstruction capability.

The remainder of this paper is arranged as follows. The related work is reviewed in section 2, the theoretical fundamentals are elaborated in section 3, the evaluation experiment is conducted in section 4, and the summary and prospect are discussed in section 5.

II. RELATED WORK

With the swift progress of deep learning theory and technology, LIC methods continuously improve their performance [22-46]. These methods can be divided into two categories: In-Training and Post-Training based methods. The former enhances LIC performance during training procedure, the latter enhances LIC performance after training procedure or during testing procedure. Both In-Training and Post-

Training methods focus on encoding-decoding network architectures, entropy models of latent representations, quantization policies, attention mechanisms, and etc.

In-Training based LIC methods utilize some state-of-the-art generative models, such as diffusion model, flow model, autoregressive model, generative adversarial network (GAN), variance autoencoder (VAE), residual network (ResNet) based model, transformer-based model, convolutional neural network (CNN) based model, and so on [22-29]. Y. C. Bai et al propose a VAE and autoregressive model based deep lossy plus residual coding method for both lossless and near-lossless image compression [22]. R. H. Yang et al present a lossy image compression approach with conditional diffusion model [23]. Y. C. Bai et al also raise an end-to-end image compression algorithm with transformer-based model [24]. Z. B. Zhang et al put forward a decoupled framework-based image compression method that lets autoregressive model hold the capability of decoding in parallel [25]. D. Y. Zhang et al come up with a resolution field-based reciprocal pyramid network for scalable image compression [26]. N. D. Jr Guerin et al propose a VAE-based LIC method that dynamically adapts loss parameters to mitigate rate estimation issues and ensure precise target bitrate attainment [27]. W. C. Zhang et al present a semantically disentangled ultra-low bitrate LIC codec by synthesizing multiple neural computing techniques such as style GAN, inverse GAN mapping, and contrastive disentangled representation learning [28]. H. S. Fu et al raise a flexible discretized Gaussian-Laplacian-Logistic mixture model for the latent representations, which can adapt to different contents in different images and different regions of one image more accurately and efficiently [29].

Some In-Training based LIC methods concentrate on quantization strategies of latent representations [30-35]. Z. H. Duan et al put forward a lossy image compression approach with quantized hierarchical VAE [30]. A. Timur comes up with a vector quantized VAE for image compression [31]. S. L. Cai et al propose a flow model based invertible continuous codec for high-fidelity variable-bitrate image compression to avoid the usage of a set of different models for compressing images at different rates [32]. H. S. Fu et al present an asymmetric LIC algorithm with multi-scale residual block, importance scaling, and post-quantization filtering

[33]. G. Zhang et al raise an enhanced quantified local implicit neural representation for image compression by enhancing the utilization of local relationships of implicit neural representation and narrow the quantization gap between training and encoding [34]. J. Y. Guo et al put forward a new LIC framework that aims to learn one single network to support variable bitrate coding under various computational complexity levels [35].

Some In-Training based LIC methods are concerned with attention mechanisms [36-38]. Z. Y. Jiang et al come up with a novel image compression autoencoder based on the local-global joint attention mechanism [36]. B. Li et al propose LIC approach via neighborhood-based attention optimization and context modeling with multi-scale guiding [37]. Z. S. Tang et al present an end-to-end image compression method integrating graph attention and asymmetric CNN [38].

Pots-Training based LIC methods strengthen the performance of pretrained LIC models [39-42]. J. Q. Shi et al adopt a plug-and-play rate-distortion optimized Post-Training quantization to process pretrained, off-the-shelf LIC models and minimize quantization-induced error of model parameters [39]. Z. H. Duan et al raise a quantization-aware ResNet VAE for lossy image compression with test-time quantization and quantization-aware training [40]. S. H. Li et al put forward a progressive LIC algorithm with dead-zone quantizers on the latent representation which is successfully incorporated into existing pretrained fixed-rate models without re-training [41]. H. Son et al come up with an enhanced standard compatible image compression framework to fuse learnable codecs, postprocessing networks, and compact representation networks [42].

Some Pots-Training based LIC methods directly enhance the quality of decoded images of LIC [43-46]. J. F. Li et al propose a recurrent convolution network for blind image compression artifact reduction in industrial IoT systems [43]. L. Ma et al present a sensitivity decouple learning approach for image compression artifacts reduction which decouples the intrinsic image attributes into compression-insensitive features for high-level semantics and compression-sensitive features for low-level cues [44]. J. H. Hu et al raise a ResNet for image compression artifact reduction [45]. H. G. Chen et al put forward a deep CNN for JPEG image compression artifacts reduction [46].

Some In-Training and Post-Training based LIC methods attempt to resolve the problem of out-of-sample, out-of-distribution, or out-of-domain testing images [7-8]. S. H. Li et al come up with a Post-Training pruning method based on the admissible range and in-distribution region to automatically remove the out-of-distribution channels for LIC [7]. K. Tsubota et al propose a content-adaptive optimization framework for universal LIC which adapts a pretrained compression model to each target image during testing for addressing the domain gap between pretraining and post-testing [8].

In summary, this paper presents a Post-Training based lossy LIC method, CIC, to minimize the discrimination between testing and training image datasets and promote the performance of image reconstruction.

III. THEORY

A. Terminology Glossary

The terminology abbreviations and mathematical notations employed in this paper are gathered in TABLE I.

TABLE I SUMMARY OF ABBREVIATIONS & NOTATIONS

Abbreviation & Notation	Meaning
EN / DE	Encoding / Decoding
SIC / CIC	Serial / Circular Image Compression
NF	Nonlinear Function
D / d	Original / Encoded Image Dimension
W / H / C	Image Width / Height / Channels
$\mathbf{f} / \mathbf{f}_e / \mathbf{f}_d$	Original / Encoded / Decoded Image
$\mathbf{f}_r / \mathbf{f}_c$	Residual Term / Control Term
$\mathbf{f}_a / \mathbf{f}_l$	Absolute / Logical Difference Image
$\mathbf{f}_t / \mathbf{f}_r$	Testing / Reference Difference Image
\mathbf{o} / \mathbf{O}	First-Order Term / Higher-Order Term
\mathbf{A} / \mathbf{U}	Coefficient Matrix
t / \mathbf{r}	Time / Reconstruction Error
N / η	Iteration Number / Iteration Constant
LIC	Learned Image Compression
VAE	Variational Auto-Encoders
DLPR	Deep Lossy Plus Residual Coding
CDC	Conditional Diffusion Compression
ICT	Image Compression with Transformers
QRVAE	Quantized ResNet Variational Auto-Encoders
VQVAE	Vector Quantized Variational Auto-Encoders
PSNR	Peak Signal-to-Noise Ratio
SSIM	Structural Similarity
BPSP	Bits Per Sub Pixel

B. Theoretical Architecture

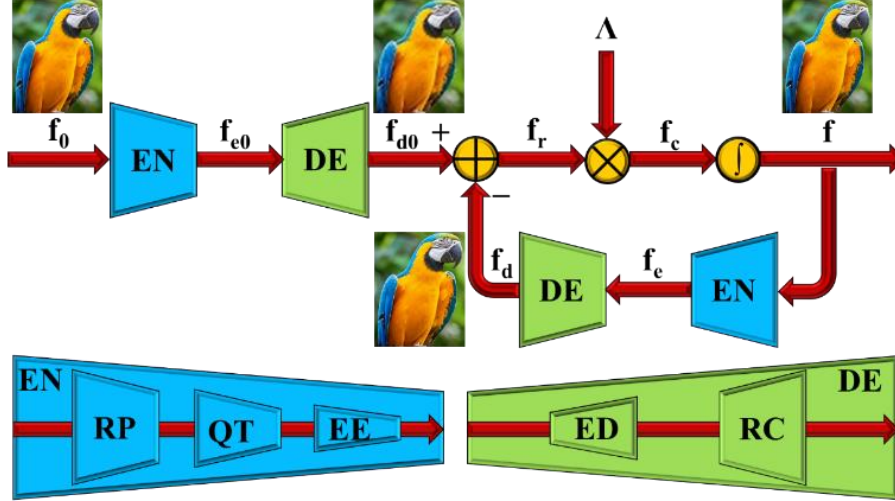


Fig. 1. The theoretical architecture of CIC.

The proposed theoretical architecture of CIC is illustrated in Figure 1. It is a combination of open-loop and closed-loop architectures. It consists of two halves: the left half and the right half. The left half is the classical open-loop SIC framework and can also be named as linked or cascade image compression. The right half is the closed-loop CIC framework and can also be named as ringed or cycle image compression. SIC contains two units: encoding (EN) and decoding (DE). The EN unit compresses the original image to the encoded image and is composed of representation (RP), quantization (QT), and entropy coding (EC). The DE unit decompresses the encoded image to the decoded image and is composed of entropy decoding (ED) and reconstruction (RC). CIC incorporates five elements: EN, DE, summator, multiplier, and integrator. The EN and DE elements of CIC are the same as those of SIC. The summator introduces negative feedback into CIC. The multiplier, integrator, and summator implement the traditional proportion-integration control. The input of the proposed architecture is original image f_0 and the output is expected reconstructed image f . The proposed CIC can achieve better reconstruction images than those of the traditional SIC.

The proposed CIC holds the property of plug-and-play and can be built on any existing advanced LIC methods. That is to say, the proposed CIC can take advantage

of the EN and DE units of any pretrained LIC models.

The SIC can be depicted by the following mathematical expressions:

$$\begin{aligned} \mathbf{f}_{e0} &= \text{EN}(\mathbf{f}_0) \\ \mathbf{f}_{d0} &= \text{DE}(\mathbf{f}_{e0}) \quad , (1) \\ \mathbf{f}_0, \mathbf{f}_{d0} &\in \mathbf{R}^D; \mathbf{f}_{e0} \in \mathbf{R}^d \end{aligned}$$

where: EN denotes the encoder and is given in the classical SIC; DE denotes the decoder and is also given in the classical SIC; \mathbf{f}_0 denotes the original image; \mathbf{f}_{e0} denotes the encoded image after EN and is the true input of the proposed architecture; \mathbf{f}_{d0} denotes the decoded image after DE; D denotes the dimension of \mathbf{f}_0 and \mathbf{f}_{d0} ; d denotes the dimension of \mathbf{f}_{e0} .

According to Equation (1), the nonlinear function (NF) of SIC from the input to the output can be portrayed by the following mathematical formulas:

$$\begin{aligned} \mathbf{f}_{d0} &= \text{DE}(\text{EN}(\mathbf{f}_0)) = \text{NF}(\mathbf{f}_0) \\ \text{NF}(\cdot) &= \text{DE}(\text{EN}(\cdot)) \quad . (2) \\ \text{NF}(\cdot) &\in \mathbf{R}^D \end{aligned}$$

The CIC can be described by the following mathematical equations:

$$\begin{aligned} \mathbf{f}_e(t) &= \text{EN}(\mathbf{f}(t)) \\ \mathbf{f}_d(t) &= \text{DE}(\mathbf{f}_e(t)) \\ \mathbf{f}_r(t) &= \mathbf{f}_{d0} - \mathbf{f}_d(t) \\ \mathbf{f}_c(t) &= \mathbf{\Lambda}(t)\mathbf{f}_r(t) \quad , (3) \\ \mathbf{f}(t) &= \mathbf{f}(0) + \int_0^t \mathbf{f}_c(t) dt \\ \mathbf{\Lambda}(t) &= \text{diag}(\mathbf{\Lambda}_{11}(t) \quad \mathbf{\Lambda}_{22}(t) \quad \cdots \quad \mathbf{\Lambda}_{DD}(t)) \\ t \in \mathbf{R}; \mathbf{f}(t), \mathbf{f}_d(t), \mathbf{f}_r(t), \mathbf{f}_c(t) &\in \mathbf{R}^D; \mathbf{f}_e(t) \in \mathbf{R}^d; \mathbf{\Lambda}(t) \in \mathbf{R}^{D \times D} \end{aligned}$$

where: t is the time; $\mathbf{f}(t)$ is the expected reconstructed image at time t and is the output of the proposed architecture; $\mathbf{f}_e(t)$ is the encoded image of $\mathbf{f}(t)$ at time t; $\mathbf{f}_d(t)$ is the decoded image of $\mathbf{f}_e(t)$ at time t; $\mathbf{f}_r(t)$ is the residual term at time t; $\mathbf{f}_c(t)$ is the control term at time t; $\mathbf{f}(0)$ is the initial value of $\mathbf{f}(t)$ at time 0 and equals zero vector, random vector, or \mathbf{f}_{d0} ; $\mathbf{\Lambda}(t)$ is the diagonal matrix of multiplication coefficient at time t; $\mathbf{\Lambda}_{ii}(t)$ is the i-th principal diagonal item of $\mathbf{\Lambda}(t)$; $\text{diag}(\cdot)$ is a diagonal matrix.

C. Loop Equation

According to Equations (2) and (3), the nonlinear loop equation of CIC can be depicted by the following mathematical expressions:

$$\begin{aligned} \mathbf{f}(t) &= \mathbf{f}(0) + \int_0^t \Lambda(t) \left(\mathbf{f}_{d0} - \text{DE}(\text{EN}(\mathbf{f}(t))) \right) dt \\ \mathbf{f}(t) &= \mathbf{f}(0) + \int_0^t \Lambda(t) \left(\mathbf{f}_{d0} - \text{NF}(\mathbf{f}(t)) \right) dt \end{aligned} \quad (4)$$

D. Nonlinear Function

The nonlinear function $\text{NF}(\mathbf{f}(t))$ in Equation (4) can be expanded with the Taylor series at \mathbf{f}_0 by the following mathematical expressions:

$$\begin{aligned} \text{NF}(\mathbf{f}(t)) &= \text{NF}(\mathbf{f}_0) + \mathbf{o}(t) + \mathbf{O}(t) \\ \mathbf{o}_i(t) &= \sum_{j=1}^D (\mathbf{f}_j(t) - \mathbf{f}_{0j}) \frac{\partial \text{NF}_i(\mathbf{f}(t))}{\partial \mathbf{f}_j(t)} \Bigg|_{\mathbf{f}(t)=\mathbf{f}_0}, \quad (5) \\ \mathbf{o}(t), \mathbf{O}(t) &\in \mathbb{R}^D; i, j = 1, 2, \dots, D \end{aligned}$$

where: $\text{NF}(\mathbf{f}_0)$ represents the constant term of $\text{NF}(\mathbf{f}(t))$ at \mathbf{f}_0 ; $\mathbf{o}(t)$ represents the first-order term of $\text{NF}(\mathbf{f}(t))$ at time t ; $\mathbf{O}(t)$ represents the second-order and higher-order term of $\text{NF}(\mathbf{f}(t))$ at time t ; $\mathbf{o}_i(t)$ represents the i -th item of $\mathbf{o}(t)$; $\mathbf{f}_j(t)$ represents the j -th item of $\mathbf{f}(t)$; \mathbf{f}_{0j} represents the j -th item of \mathbf{f}_0 ; $\text{NF}_i(\mathbf{f}(t))$ represents the i -th item of $\text{NF}(\mathbf{f}(t))$.

For the purpose of subsequent theoretical analysis, after abandoning the second-order and higher-order term $\mathbf{O}(t)$, the $\text{NF}(\mathbf{f}(t))$ can be approximated by the following linear function:

$$\text{NF}(\mathbf{f}(t)) \approx \text{NF}(\mathbf{f}_0) + \mathbf{o}(t). \quad (6)$$

The linear term $\mathbf{o}_i(t)$ can be further approximated by the following mathematical formulas:

$$\mathbf{o}_i(t) \approx (\mathbf{f}_i(t) - \mathbf{f}_{0i}) \frac{\partial \text{NF}_i(\mathbf{f})}{\partial \mathbf{f}_i(t)} \Bigg|_{\mathbf{f}_i(t)=\mathbf{f}_{0i}}, \quad i = 1, 2, \dots, D. \quad (7)$$

According to Equation (7), the linear term $\mathbf{o}(t)$ can be adapted by the following equations:

$$\begin{aligned}
\mathbf{o}(t) &\approx \mathbf{U}(t)(\mathbf{f}(t) - \mathbf{x}_0) \\
\mathbf{U}(t) &= \text{diag}(\mathbf{U}_{11}(t) \quad \mathbf{U}_{22}(t) \quad \cdots \quad \mathbf{U}_{DD}(t)) \\
\mathbf{U}_{ii}(t) &= \left. \frac{\partial \text{NF}_i(\mathbf{f}(t))}{\partial \mathbf{f}_i(t)} \right|_{\mathbf{f}(t)=\mathbf{f}_0}, \quad (8) \\
\mathbf{U}(t) &\in \mathbb{R}^{D \times D}; i = 1, 2, \dots, D
\end{aligned}$$

where: $\mathbf{U}(t)$ denotes the coefficient matrix at time t ; $\mathbf{U}_{ii}(t)$ denotes the i -th principal diagonal element of $\mathbf{U}(t)$.

E. Steady-State Error

The reconstruction error between the expected reconstruction image $\mathbf{f}(t)$ and the original image \mathbf{f}_0 can be depicted by the following mathematical expression:

$$\mathbf{r}(t) = \mathbf{f}(t) - \mathbf{f}_0, \mathbf{r}(t) \in \mathbb{R}^D. \quad (9)$$

According to Equation (4), the expected reconstruction image $\mathbf{f}(t)$ at time $t+\Delta t$ can be portrayed by the following mathematical formula:

$$\begin{aligned}
\mathbf{f}(t+\Delta t) &= \mathbf{f}(t) + \int_t^{t+\Delta t} \mathbf{\Lambda}(t)(\mathbf{f}_{d0} - \text{NF}(\mathbf{f}(t))) dt \quad (10) \\
&\text{s.t. } \Delta t > 0
\end{aligned}$$

Subtracting \mathbf{f}_0 from both sides of Equation (10), the following mathematical equation can be gained:

$$\mathbf{f}(t+\Delta t) - \mathbf{f}_0 = \mathbf{f}(t) - \mathbf{f}_0 + \int_t^{t+\Delta t} \mathbf{\Lambda}(t)(\mathbf{f}_{d0} - \text{NF}(\mathbf{f}(t))) dt \quad (11)$$

According to Equation (9), the following mathematical expressions can be acquired:

$$\begin{aligned}
\mathbf{r}(t+\Delta t) &= \mathbf{r}(t) + \int_t^{t+\Delta t} \mathbf{\Lambda}(t)(\mathbf{f}_{d0} - \text{NF}(\mathbf{f}(t))) dt \quad (12) \\
\mathbf{r}(t+\Delta t) &= \mathbf{f}(t+\Delta t) - \mathbf{f}_0
\end{aligned}$$

where $\mathbf{r}(t+\Delta t)$ means the error vector at time $t+\Delta t$.

If Δt approaches zero, Equation (12) can be approximated by the following mathematical formula:

$$\begin{aligned}
\mathbf{r}(t+\Delta t) &\approx \mathbf{r}(t) + \mathbf{\Lambda}(t)(\mathbf{f}_{d0} - \text{NF}(\mathbf{f}(t))) \Delta t \quad (13) \\
&\text{s.t. } \Delta t \rightarrow 0
\end{aligned}$$

According to Equations (2), (6), (8), and (9), the following mathematical

equations can be achieved:

$$\begin{aligned}\mathbf{r}(t+\Delta t) &\approx \mathbf{r}(t) - \Lambda(t)\mathbf{o}(t)\Delta t \approx \mathbf{r}(t) - \Lambda(t)\mathbf{U}(t)(\mathbf{f}(t) - \mathbf{f}_0)\Delta t \\ &= \mathbf{r}(t) - \Lambda(t)\mathbf{U}(t)\mathbf{r}(t)\Delta t = (\mathbf{I} - \Lambda(t)\mathbf{U}(t)\Delta t)\mathbf{r}(t) \\ &= (\mathbf{I} - \Delta t\Lambda(t)\mathbf{U}(t))\mathbf{r}(t)\end{aligned}\quad , (14)$$

where \mathbf{I} denotes the unit matrix.

Calculating norm in both sides of Equation (14), the following mathematical inequation can be gained:

$$\|\mathbf{r}(t+\Delta t)\|_2 \leq \|\mathbf{I} - \Delta t\Lambda(t)\mathbf{U}(t)\|_F \cdot \|\mathbf{r}(t)\|_2, \quad (15)$$

where: subscript 2 represents 2-norm; subscript F represents Frobenius-norm.

We can always select proper $\Lambda(t)$ and $\mathbf{U}(t)$ to meet the following inequality:

$$\|\mathbf{I} - \Delta t\Lambda(t)\mathbf{U}(t)\|_F < 1. \quad (16)$$

For instance, $\Lambda(t)$ and $\mathbf{U}(t)$ are respectively proportional to a unit matrix:

$$\begin{aligned}\Lambda(t) &= \eta\mathbf{I}, \mathbf{U}(t) = \mu(t)\mathbf{I} \\ \mu(t) &= \frac{1}{D} \sum_{i=1}^D \mathbf{U}_{ii}(t) = \frac{1}{D} \sum_{i=1}^D \left. \frac{\partial \text{NF}_i(\mathbf{f}(t))}{\partial \mathbf{f}_i(t)} \right|_{\mathbf{r}(t)=\mathbf{f}_0}, \quad (17)\end{aligned}$$

where: η denotes a constant; $\mu(t)$ denotes the average of $\mathbf{U}_{ii}(t)$ in Equation (8).

According to Equation (17), we can always seek out a suitable η to satisfy Inequation (16):

$$\begin{aligned}\|\mathbf{I} - \Delta t\Lambda(t)\mathbf{U}(t)\|_F &= \|\mathbf{I} - \Delta t \cdot \eta\mathbf{I} \cdot \mu(t)\mathbf{I}\|_F = \|(1 - \Delta t \cdot \eta \cdot \mu(t))\mathbf{I}\|_F \\ &= |1 - \Delta t \cdot \eta \cdot \mu(t)| \cdot \|\mathbf{I}\|_F = |1 - \Delta t \cdot \eta \cdot \mu(t)| \cdot \sqrt{D} < 1 \quad . (18) \\ \Rightarrow &\begin{cases} \frac{1 - \frac{1}{\sqrt{D}}}{\Delta t \cdot \mu(t)} < \eta < \frac{1 + \frac{1}{\sqrt{D}}}{\Delta t \cdot \mu(t)}, \mu(t) > 0 \\ \frac{1 + \frac{1}{\sqrt{D}}}{\Delta t \cdot \mu(t)} < \eta < \frac{1 - \frac{1}{\sqrt{D}}}{\Delta t \cdot \mu(t)}, \mu(t) < 0 \end{cases}\end{aligned}$$

According to Equations (15) and (16), the following mathematical inequality can be acquired:

$$\|\mathbf{r}(t+\Delta t)\|_2 < \|\mathbf{r}(t)\|_2. \quad (19)$$

According to Inequation (19), if time t is approximate to infinite in steady-state, the reconstruction error is close to zero, and $\mathbf{f}(t)$ approximates to \mathbf{f}_0 . It can be portrayed by the following mathematical limit:

$$\begin{aligned} \lim_{t \rightarrow \infty} \mathbf{r}(t) &= \lim_{t \rightarrow \infty} (\mathbf{f}(t) - \mathbf{f}_0) = 0 \\ \lim_{t \rightarrow \infty} \mathbf{f}(t) &= \mathbf{f}_0 \end{aligned} \quad . \quad (20)$$

Hence, the proposed CIC can obtain the perfect reconstruction image $\mathbf{f}(t)$ which is approximate to the original image \mathbf{f}_0 .

F. Algorithm Description

The proposed CIC algorithm is described in Algorithm 1, where N is the total number of iterations.

Algorithm 1: CIC.

Input: \mathbf{f}_0
Initialization:
 $\mathbf{n} = 1, \mathbf{f}_{d0} = \mathbf{NF}(\mathbf{f}_0), \mathbf{f} = \mathbf{0}, \mathbf{f}_{d0}$, or random vector
while $\mathbf{n} \leq N$
 update \mathbf{f} according to equation (4), (6), (11) and (17)
 $\mathbf{n} = \mathbf{n} + 1$
end
Output: \mathbf{f}

IV. EXPERIMENT

A. Experimental Conditions

Five public image compression datasets, Kodak, CLIC2021 Test, CLIC2021 Validation, CLIC2022 Validation, and CLIC2024 Validation, are utilized to evaluate the performance of LIC methods. These image datasets are enumerated in TABLE II including the total number of images, the resolution of images, and the web link of image datasets.

Five competing open-source methods of SIC, Deep Lossy Plus Residual Coding (DLPR) [22], Conditional Diffusion Compression (CDC) [23], Image Compression with Transformers (ICT) [24], Quantized ResNet VAE (QRVAE) [30], and Vector

Quantized VAE (VQVAE) [31], are adopted for comparison with the proposed CIC method. These methods are listed in TABLE III including algorithm names and web links. Because the proposed CIC method has the property of plug-and-play and Post-Training, five CIC versions of the competing methods, circular DLPR (CDLPR), circular CDC (CCDC), circular ICT (CICT), circular QRVAE (CQRVAE), and circular VQVAE (CVQVAE), are presented for comparison.

TABLE II IMAGE DATASETS

Dataset	Detail	
Kodak	Number	24
	Resolution	768×512
	Link	https://www.kaggle.com/datasets/sherylmehta/kodak-dataset
CLIC2021 Test	Number	60
	Resolution	$751 \times 500 \sim 2048 \times 1400$
	Link	https://clic.compression.cc/2021/tasks/index.html
CLIC2021 Validation	Number	41
	Resolution	$512 \times 384 \sim 2048 \times 1370$
	Link	https://clic.compression.cc/2021/tasks/index.html
CLIC2022 Validation	Number	30
	Resolution	$1151 \times 2048 \sim 2048 \times 2048$
	Link	https://clic.compression.cc/2022/
CLIC2024 Validation	Number	30
	Resolution	$1152 \times 2048 \sim 2048 \times 2048$
	Link	https://compression.cc/tasks/

TABLE III COMPETING METHODS

Method	Link
DLPR	https://github.com/BYchao100/Deep-Lossy-Plus-Residual-Coding
CDC	https://github.com/buggyyang/CDC_compression
ICT	https://github.com/BYchao100/Towards-Image-Compression-and-Analysis-with-Transformers
QRVAE	https://github.com/duanzhihao/qres-vae
VQVAE	https://github.com/TimeEscaper/vq-vic

Three simulation experiments, quantization parameter, reconstruction performance, and out-of-sample, are designed to compare the performance between the conventional SIC and the proposed CIC.

Three performance metrics, PSNR, SSIM, and BPSP, are selected to assess the capability of SIC and CIC. For reconstruction image \mathbf{f} and original image \mathbf{f}_0 , the definitions of PSNR, SSIM, and BPSP are depicted by the following mathematical expressions:

$$\text{PSNR}(\mathbf{f}, \mathbf{f}_0) = 10 \lg \left(\frac{255^2}{\frac{1}{D} \sum_{i=1}^D (\mathbf{f}_i - \mathbf{f}_{0i})^2} \right), \quad (21)$$

$$\text{SSIM}(\mathbf{f}, \mathbf{f}_0) = \frac{(2\mu_f \mu_{f_0} + (0.01 \times 255)^2)(2\sigma_{ff_0} + (0.03 \times 255)^2)}{(\mu_f^2 + \mu_{f_0}^2 + (0.01 \times 255)^2)(\sigma_f^2 + \sigma_{f_0}^2 + (0.03 \times 255)^2)}, \quad (22)$$

$$\text{BPSP} = \frac{B}{S \times W \times H \times C}, \quad (23)$$

where: \mathbf{f}_i denotes the i -th element of \mathbf{f} ; \mathbf{f}_{0i} denotes the i -th element of \mathbf{f}_0 ; μ_f denotes the element-wise mean of \mathbf{f} ; μ_{f_0} denotes the element-wise mean of \mathbf{f}_0 ; σ_f denotes the element-wise standard deviation of \mathbf{f} ; σ_{f_0} denotes the element-wise standard deviation of \mathbf{f}_0 ; σ_{ff_0} denotes the element-wise covariance of \mathbf{f} and \mathbf{f}_0 ; B denotes the total number of bits for an image; S denotes the total number of bits for a subpixel; W denotes the width of an image; H denotes the height of an image; C denotes the total number of channels of an image.

For the purpose of comparing the difference between the reconstruction images of SIC and CIC, absolute difference image and logic difference image are defined by the following mathematical formulas:

$$\begin{aligned} \mathbf{f}_a(i, j) &= |\mathbf{f}_t(i, j) - \mathbf{f}_r(i, j)| \\ \mathbf{f}_l(i, j) &= \begin{cases} 1, & |\mathbf{f}_t(i, j) - \mathbf{f}_r(i, j)| > T \\ 0, & |\mathbf{f}_t(i, j) - \mathbf{f}_r(i, j)| \leq T \end{cases}, \quad (24) \\ \mathbf{f}_a, \mathbf{f}_l, \mathbf{f}_t, \mathbf{f}_r &\in \mathbb{R}^{H \times W}; i, j \in Z; T \in \mathbb{R} \end{aligned}$$

where: \mathbf{f}_a means the absolute difference image; \mathbf{f}_l means the logic difference image; \mathbf{f} means the testing image; \mathbf{f}_r means the reference image; i means the row index of an image; j means the column index of an image; T means a threshold.

The experimental hardware platforms contain Intel CPU and Nvidia GPU. The experimental software platforms contain Google TensorFlow, FaceBook PyTorch, Microsoft COLAB, and MathWorks MATLAB running on Windows or Linux operating systems. Detailed hardware and software configurations are listed in TABLE IV.

TABLE IV DETAILED HARDWARE AND SOFTWARE CONFIGURATIONS

Hardware Configurations	
Item	Value
CPU Type	Intel Core i7
CPU Memory	8GB
GPU Type	NVIDIA Tesla V100
GPU Memory	16GB
Software Configurations	
Item	Value
Input/Output Channels	3/3
Batch Size	1
Block Size	64×64
Iteration Number (N)	1~10
Iteration Constant (η)	-1~+1

B. Experimental Results

1) Experimental Results of Quantization Parameter

This experiment is designed to investigate the relationship between the performance of image compression and the quantization parameter. This experiment focuses on the DLPR and CDLPR algorithms and the single image, kodim01.png, of Kodak image dataset. It is shown in Figure 2 that PSNR decreases while quantization parameter τ increases and CDLPR outperforms DLPR in PSNR. It is also displayed in Figure 3 that SSIM decreases while quantization parameter τ increases and CDLPR exceeds DLPR in SSIM. It is further illustrated in Figure 4 that BPSP decreases while quantization parameter τ increases and CDLPR surpasses DLPR in BPSP.

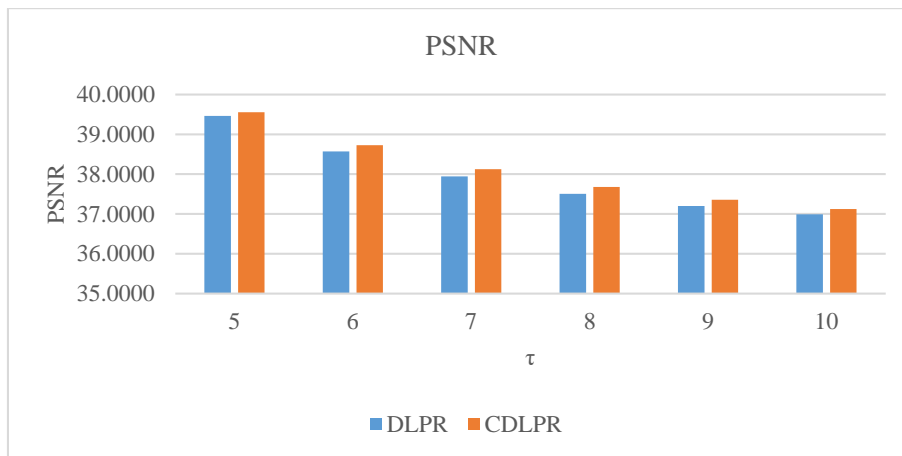


Fig. 2. PSNR of DLPR and CDLPR on single image of Kodak image dataset.

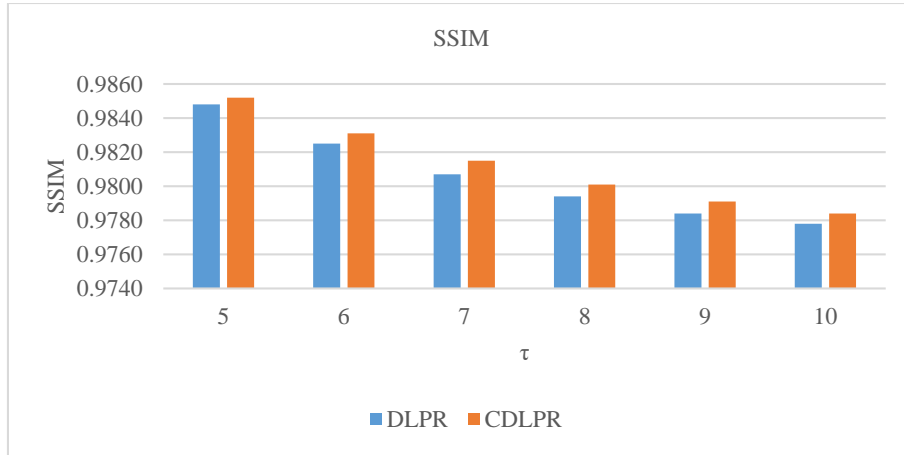


Fig. 3. SSIM of DLPR and CDLPR on single image of Kodak image dataset.

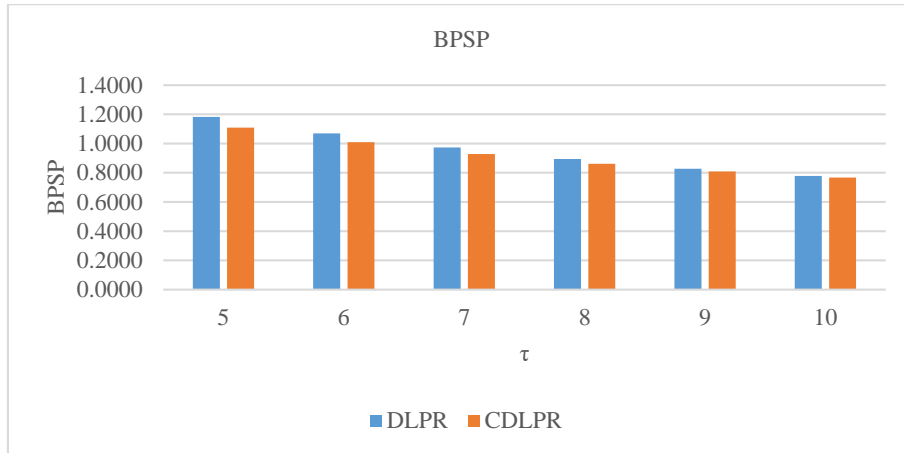


Fig. 4. BPSP of DLPR and CDLPR on single image of Kodak image dataset.

2) Experimental Results of Reconstruction Performance

This experiment is planned to compare the reconstruction performance between the traditional SIC and the proposed CIC. This experiment concentrates on five competing open-source methods and five public image datasets.

Figures 5, 6, and 7 demonstrate the PSNR, SSIM, and BPSP of DLPR and CDLPR algorithms with quantization parameter $\tau=7$ on Kodak image dataset. The experimental results indicate that the proposed CDLPR is superior to the classical DLPR in PSNR, SSIM, and BPSP.

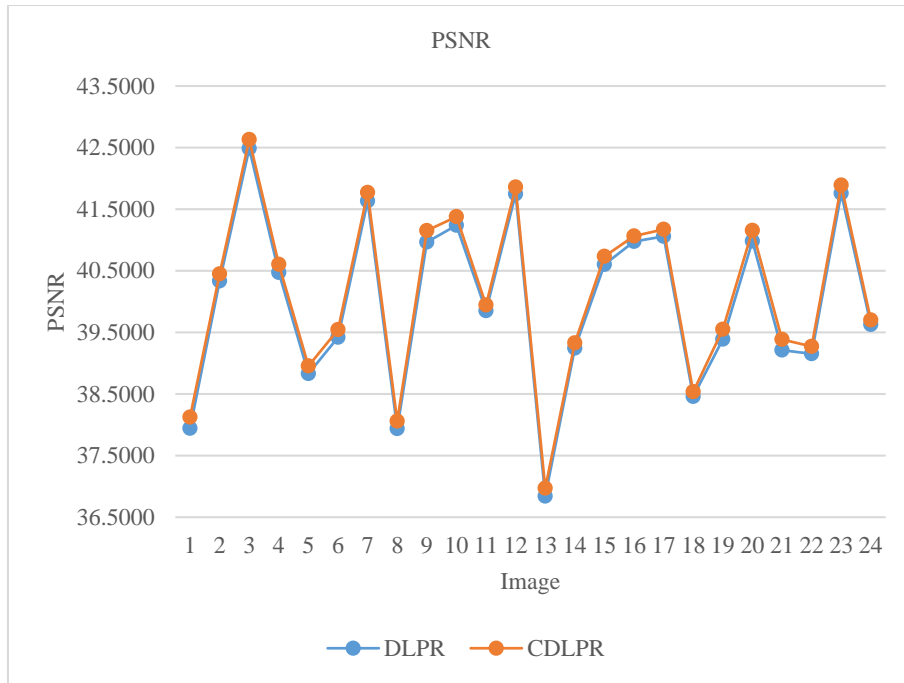


Fig. 5. PSNR of DLPR and CDLPR on Kodak image dataset.

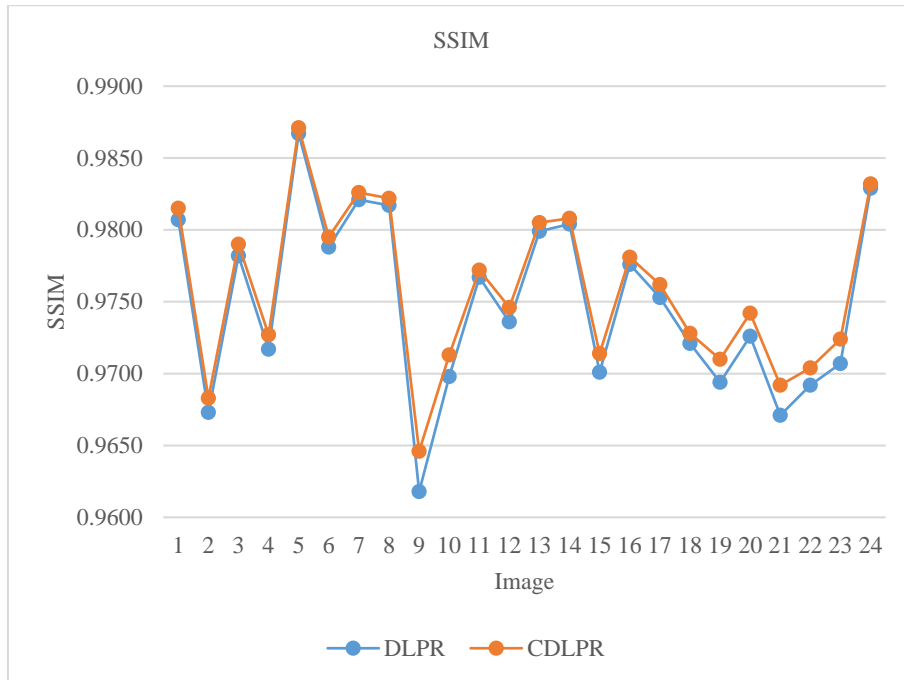


Fig. 6. SSIM of DLPR and CDLPR on Kodak image dataset.

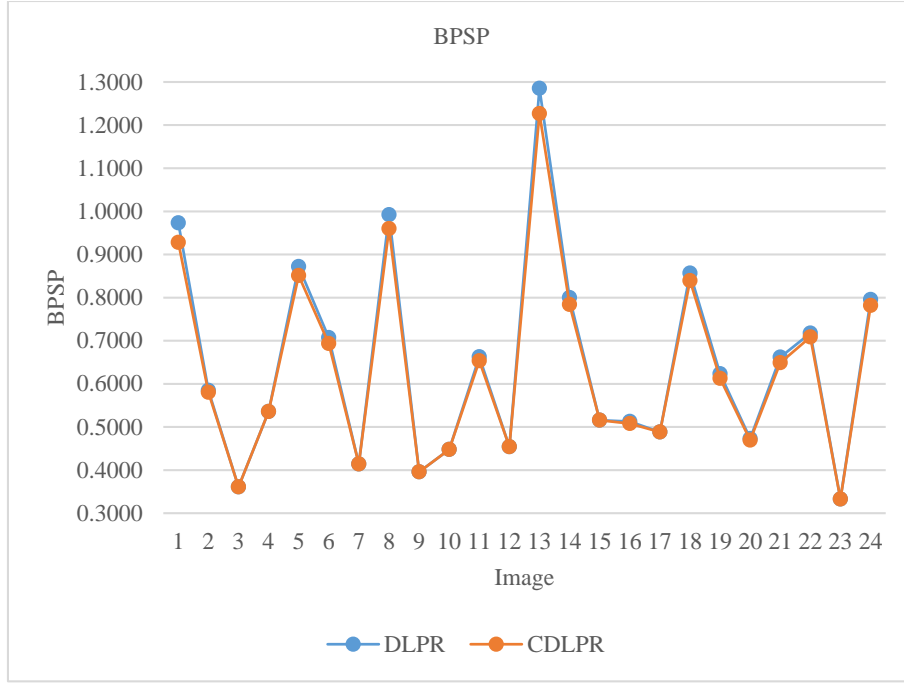


Fig. 7. BPSD of DLPR and CDLPR on Kodak image dataset.

TABLE V shows the PSNR, SSIM, and BPSD of DLPR and CDLPR with quantization parameter $\tau=7$ on five image datasets. The PSNR, SSIM, and BPSD are the averages on each dataset. Δ is the average increment of PSNR or SSIM between CDLPR and DLPR on each dataset. Δ_m is the maximum increment of PSNR or SSIM between CDLPR and DLPR on each dataset. Δ is also the average decrement of BPSD between CDLPR and DLPR on each dataset. Δ_m is also the maximum decrement of BPSD between CDLPR and DLPR on each dataset. The maximum PSNR increment is 1.7142 dB on CLIC2021 Test image dataset. The experimental results manifest that the proposed CDLPR holds superiority over the classical DLPR in PSNR, SSIM, and BPSD.

TABLE VI displays the PSNR, SSIM, and BPSD of CDC and CCDC with quantization parameter 0.0128 on five image datasets. The maximum PSNR increment is 5.7129 dB on CLIC2021 Test image dataset. For the convenience of computation, some images are clipped to the same size as images of Kodak image dataset. The experimental results reveal that the proposed CCDC overbalances the classical CDC in PSNR and SSIM while both of them have the same BPSR.

TABLE VII illustrates the PSNR, SSIM, and BPSR of ICT and CICT with quantization parameter 3 on five image datasets. The maximum PSNR increment is 2.7907 dB on CLIC2021 Test image dataset. For the expediency of calculation, some images are trimmed to the same size as images of Kodak image dataset. The experimental results uncover that the proposed CICT overmatches the classical ICT in PSNR, SSIM, and BPSR.

TABLE VIII demonstrates the PSNR, SSIM, and BPSR of QRVAE and CQRVAE with quantization parameter 16 on five image datasets. The maximum PSNR increment is 4.9347 dB on CLIC2021 Test image dataset. For the facilitation of implementation, some images are tailored to the same size of images of Kodak image dataset. The experimental results indicate that the proposed CQRVAE outperforms the classical QRVAE in PSNR and SSIM while both of them have the same BPSR.

TABLE IX exhibits the PSNR, SSIM, and BPSR of VQVAE and CVQVAE on five image datasets. The maximum PSNR increment is 1.5219 dB on CLIC2021 Validation image dataset. For the easiness of realization, some images are cropped to the same size as images of Kodak image dataset. The experimental results make clear that the proposed CVQVAE surpasses the classical VQVAE in PSNR and SSIM while both of them have the same BPSR.

TABLE V EXPERIMENTAL RESULTS OF DLPR AND CDLPR ON FIVE IMAGE DATASETS

Dataset		Kodak	CLIC2021 Test	CLIC2021 Validation	CLIC2022 Validation	CLIC2024 Validation
PSNR↑	DLPR	40.0063	41.3359	40.5765	41.0578	40.2871
	CDLPR	40.1345	41.5588	40.7525	41.2347	40.4597
	Δ	0.1282	0.2229	0.1760	0.1769	0.1726
	Δ_m	0.1861	1.7142	0.4736	0.3763	0.3537
SSIM↑	DLPR	0.9749	0.9711	0.9668	0.9714	0.9702
	CDLPR	0.9759	0.9739	0.9689	0.9728	0.9722
	Δ	0.0010	0.0027	0.0021	0.0014	0.0019
	Δ_m	0.0028	0.0388	0.0129	0.0054	0.0110
BPSR↓	DLPR	0.6443	0.4610	0.5089	0.5436	0.5920
	CDLPR	0.6329	0.4541	0.4999	0.5312	0.5802
	Δ	0.0114	0.0069	0.0090	0.0123	0.0119
	Δ_m	0.0585	0.0565	0.0577	0.0803	0.0522

TABLE VI EXPERIMENTAL RESULTS OF CDC AND CCDC ON FIVE IMAGE DATASETS

Dataset		Kodak	CLIC2021 Test	CLIC2021 Validation	CLIC2022 Validation	CLIC2024 Validation
PSNR↑	CDC	34.3532	38.2491	36.8646	37.0497	36.7745
	CCDC	34.4227	38.7852	37.0708	37.6947	37.0449

SSIM \uparrow	Δ	0.0694	0.5361	0.2062	0.6450	0.2704
	Δ_m	0.1448	5.7129	1.8855	2.8527	2.8118
	CDC	0.9379	0.9447	0.9364	0.9409	0.9387
	CCDC	0.9382	0.9466	0.9373	0.9417	0.9405
	Δ	0.0003	0.0019	0.0009	0.0008	0.0018
	Δ_m	0.0015	0.0503	0.0144	0.0095	0.0131
BPSP \downarrow	CDC	0.8389	0.3926	0.5368	0.4751	0.4815
	CCDC	0.8389	0.3926	0.5368	0.4751	0.4815
	Δ	0.0000	0.0000	0.0000	0.0000	0.0000
	Δ_m	0.0000	0.0000	0.0000	0.0000	0.0000

TABLE VII EXPERIMENTAL RESULTS OF ICT AND CICT ON FIVE IMAGE DATASETS

Dataset		Kodak	CLIC2021 Test	CLIC2021 Validation	CLIC2022 Validation	CLIC2024 Validation
PSNR \uparrow	ICT	29.4609	29.1243	29.6862	29.3554	28.1825
	CICT	29.5614	29.2873	29.7799	29.4643	28.2794
	Δ	0.1005	0.1630	0.0936	0.1089	0.0969
	Δ_m	0.2573	2.7907	0.2281	0.2830	0.2254
SSIM \uparrow	ICT	0.7191	0.7994	0.7812	0.7940	0.7931
	CICT	0.7254	0.8042	0.7856	0.7984	0.7979
	Δ	0.0062	0.0048	0.0045	0.0045	0.0048
	Δ_m	0.0112	0.0237	0.0107	0.0142	0.0305
BPSP \downarrow	ICT	0.4007	0.3947	0.3445	0.4665	0.5397
	CICT	0.3313	0.3891	0.3395	0.4058	0.4683
	Δ	0.0694	0.0056	0.0049	0.0607	0.0715
	Δ_m	0.1378	0.0976	0.1155	0.1097	0.1148

TABLE VIII EXPERIMENTAL RESULTS OF QRVAE AND CQRVAE ON FIVE IMAGE DATASETS

Dataset		Kodak	CLIC2021 Test	CLIC2021 Validation	CLIC2022 Validation	CLIC2024 Validation
PSNR \uparrow	QRVAE	30.0170	34.0337	32.3537	33.4110	32.6968
	CQRVAE	30.9856	35.2369	33.3826	34.4798	33.8661
	Δ	0.9686	1.2032	1.0289	1.0688	1.1693
	Δ_m	1.2953	4.9347	2.5864	4.3077	3.6048
SSIM \uparrow	QRVAE	0.8093	0.8937	0.8625	0.8856	0.8873
	CQRVAE	0.8599	0.9102	0.8887	0.9013	0.9050
	Δ	0.0506	0.0164	0.0262	0.0157	0.0177
	Δ_m	0.0966	0.0991	0.1094	0.1028	0.0533
BPSP \downarrow	QRVAE	0.1829	0.0653	0.1008	0.0948	0.0860
	CQRVAE	0.1829	0.0653	0.1008	0.0948	0.0860
	Δ	0.0000	0.0000	0.0000	0.0000	0.0000
	Δ_m	0.0000	0.0000	0.0000	0.0000	0.0000

TABLE IX EXPERIMENTAL RESULTS OF VQVAE AND CVQVAE ON FIVE IMAGE DATASETS

Dataset		Kodak	CLIC2021 Test	CLIC2021 Validation	CLIC2022 Validation	CLIC2024 Validation
PSNR \uparrow	VQVAE	32.1650	32.5532	32.8301	32.6257	33.1952
	CVQVAE	32.5840	32.9286	33.2335	32.9414	33.5463
	Δ	0.4190	0.3755	0.4034	0.3157	0.3511
	Δ_m	1.1633	0.8489	1.5219	1.2535	0.8269
SSIM \uparrow	VQVAE	0.9657	0.9613	0.9578	0.9685	0.9576
	CVQVAE	0.9663	0.9626	0.9586	0.9690	0.9601

	Δ	0.0006	0.0013	0.0009	0.0005	0.0025
	Δ_m	0.0020	0.0195	0.0082	0.0021	0.0397
BPSP↓	VQVAE	0.9936	0.6831	0.7546	0.7986	0.8077
	CVQVAE	0.9936	0.6831	0.7546	0.7986	0.8077
	Δ	0.0000	0.0000	0.0000	0.0000	0.0000
	Δ_m	0.0000	0.0000	0.0000	0.0000	0.0000

In order to explicitly show the performance difference of image reconstruction between the proposed CIC and the classical SIC, some example images are displayed in Figures 8 to 12.

Figure 8 shows the experimental results of DLPR and CDLPR with maximum PSNR increment on Kodak image dataset. Figure 8(a) is the original image, Figure 8(b) is the reconstruction image of DLPR, and Figure 8(c) is the reconstruction image of CDLPR. It is hard to discover the difference between Figure 8(b) and Figure 8(c). Figure 8(d) is the subblock of Figure 8(a), Figure 8(e) is the related subblock of Figure 8(b), and Figure 8(f) is the related subblock of Figure 8(c). Figure 8(d), (e), and (f) are marked with red boxes in Figure 8(a), (b), and (c) respectively. It is also hard to discover the difference between Figure 8(e) and Figure 8(f). Figure 8(g) is the absolute difference image block between Figure 8(e) and Figure 8(d), and Figure 8(h) is the absolute difference image block between Figure 8(f) and Figure 8(d). It is still hard to discover the difference between Figure 8(g) and Figure 8(h). Figure 8(i) is the logic difference image block between Figure 8(e) and Figure 8(d), and Figure 8(j) is the logic difference image block between Figure 8(f) and Figure 8(d). It is easy to discover the difference between Figure 8(i) and Figure 8(j). Figure 8(i) and Figure 8(j) indicate that the reconstruction image quality of CDLPR outperforms that of DLPR. Figure 8 indicates that the proposed method is effective for testing images with sharp edges.

Figure 9 displays the experimental results of DLPR and CDLPR with maximum PSNR rise on CLIC2021 test image dataset. The layout of Figure 9 is same as Figure 8. It is difficult to seek out the discrepancy between Figure 9(b) and Figure 9(c); It is also difficult to seek out the discrepancy between Figure 9(e) and Figure 9(f); It is still difficult to seek out the discrepancy between Figure 9(g) and Figure 9(h); It is effortless to seek out the discrepancy between Figure 9(i) and Figure 9(j). Figure 9(i) and Figure 9(j) reveal that the restoration image quality of CDLPR

outbalances that of DLPR. Figure 9 shows that the proposed method is propitious to testing images with dark and high contrast.

Figure 10 illustrates the experimental results of DLPR and CDLPR with maximum PSNR increase on CLIC2021 validation image dataset. The composition of Figure 10 is same as Figure 8. It is tough to check the discrimination between Figure 10(b) and Figure 10(c); It is also tough to check the discrimination between Figure 10(e) and Figure 10(f); It is still tough to check the discrimination between Figure 10(g) and Figure 10(h); It is toil-less to check the discrimination between Figure 10(i) and Figure 10(j). Figure 10(i) and Figure 10(j) uncover that the recovery image quality of CDLPR overmatches that of DLPR. Figure 10 demonstrates that the proposed method is appropriate for testing images with grid shapes.

Figure 11 demonstrates the experimental results of DLPR and CDLPR with maximum PSNR improvement on CLIC2022 validation image dataset. The arrangement of Figure 11 is same as Figure 8. It is arduous to examine the distinction between Figure 11(b) and Figure 11(c); It is also arduous to examine the distinction between Figure 11(e) and Figure 11(f); It is still arduous to examine the distinction between Figure 11(g) and Figure 11(h); It is convenient to examine the distinction between Figure 11(i) and Figure 11(j). Figure 11(i) and Figure 11(j) disclose that the reestablishment image quality of CDLPR exceeds that of DLPR. Figure 11 indicates that the proposed method is fit for testing images with dark backgrounds and high contrast.

Figure 12 exhibits the experimental results of DLPR and CDLPR with maximum PSNR gain on CLIC2024 validation image dataset. The organization of Figure 12 is same as Figure 8. It is formidable to inspect the distinguishing between Figure 12(b) and Figure 12(c); It is also formidable to inspect the distinguishing between Figure 12(e) and Figure 12(f); It is still formidable to inspect the distinguishing between Figure 12(g) and Figure 12(h); It is facile to inspect the distinguishing between Figure 12(i) and Figure 12(j). Figure 12(i) and Figure 12(j) expose that the rebuilding image quality of CDLPR surpasses that of DLPR. Figure 12 shows the proposed method is suitable for testing images with complicated patterns.

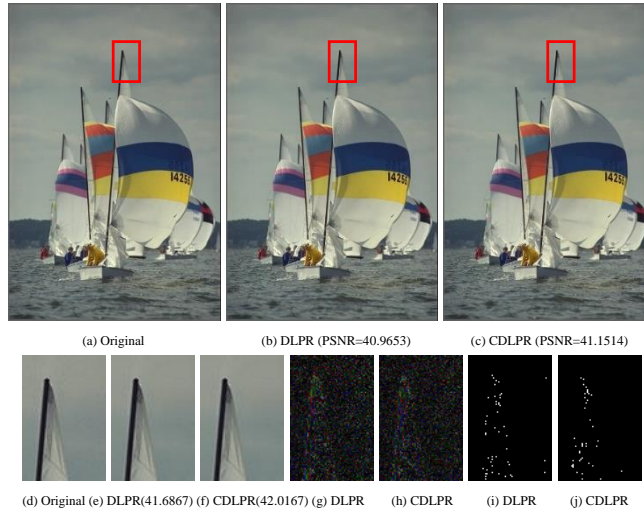


Fig. 8. Experimental results of DLPR and CDLPR with maximum PSNR increment on Kodak image dataset.



Fig. 9. Experimental results of DLPR and CDLPR with maximum PSNR increment on CLIC2021 test image dataset.

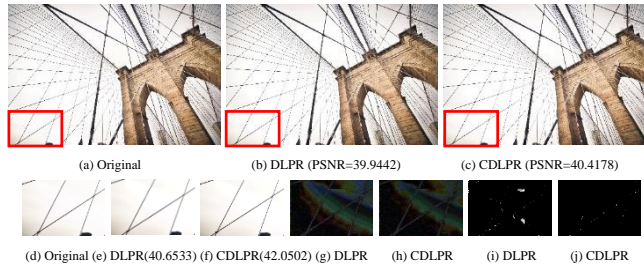


Fig. 10. Experimental results of DLPR and CDLPR with maximum PSNR increment on CLIC2021 validation image dataset.

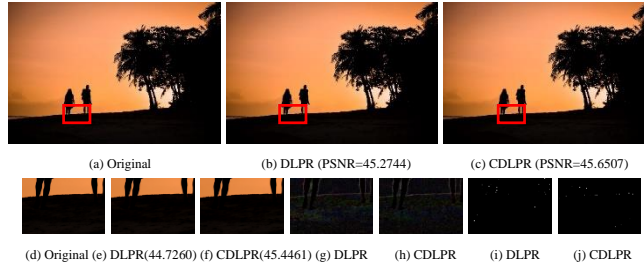


Fig. 11. Experimental results of DLPR and CDLPR with maximum PSNR increment on CLIC2022 validation image dataset.

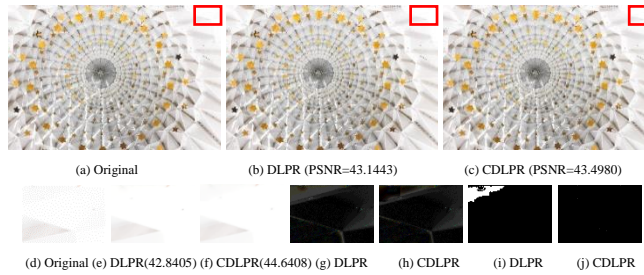


Fig. 12. Experimental results of DLPR and CDLPR with maximum PSNR increment on CLIC2024 validation image dataset.

Therefore, the proposed CIC holds superiority over the classical SIC in reconstruction performance and is especially appropriate for testing images with sharp edges, dark backgrounds, high contrast, grid shapes, and complicated patterns.

3) Experiment Results of Out-of-Sample

TABLE X EXPERIMENTAL RESULTS OF DLPR AND CDLPR FOR OUT-OF-SAMPLE TESTING IMAGES

Testing Images		1	2	3	4	5
PSNR \uparrow	DLPR	42.0104	42.0685	41.5296	40.7594	42.7895
	CDLPR	42.9432	42.7137	41.9656	41.7546	43.3530
	Δ	0.9329	0.6452	0.4361	0.9953	0.5635
	Δ_s	1.1742	0.9036	0.7093	2.4978	1.0996
SSIM \uparrow	DLPR	0.9818	0.9308	0.8477	0.8731	0.9850
	CDLPR	0.9885	0.9460	0.8599	0.9088	0.9888
	Δ	0.0067	0.0152	0.0122	0.0357	0.0039
	Δ_s	0.0111	0.0421	0.0221	0.0314	0.0068
BPSP \downarrow	DLPR	0.4892	0.5833	0.2888	0.5056	0.6678
	CDLPR	0.4840	0.5692	0.2851	0.4986	0.6633
	Δ	0.0052	0.0141	0.0037	0.0070	0.0045

This experiment is arranged to assess the reconstruction performance for out-of-sample testing images. Five typical out-of-sample testing images are selected in

Figures 13 to 17. DLPR and CDLPR algorithms with quantization parameter $\tau=7$ are chosen for performance comparison. The experimental results are listed in TABLE X and shown in Figures 13 to 17.

Figure 13 offers the experimental results of out-of-sample testing image 1. Figure 13(a) is the original image, Figure 13(b) is the reconstruction image of DLPR, and Figure 13(c) is the reconstruction image of CDLPR. It is untoward to survey the difference between Figure 13(b) and Figure 13(c). Figure 13(d) is the subblock of Figure 13(a), Figure 13(e) is the related subblock of Figure 13(b), and Figure 13(f) is the related subblock of Figure 13(c). Figure 13(d), (e), and (f) are marked with red boxes in Figure 13(a), (b), and (c) respectively. It is also untoward to survey the difference between Figure 13(e) and Figure 13(f). Figure 13(g) is the absolute difference image block between Figure 13(e) and Figure 13(d), and Figure 13(h) is the absolute difference image block between Figure 13(f) and Figure 13(d). It is still untoward to survey the difference between Figure 13(g) and Figure 13(h). Figure 13(i) is the logic difference image block between Figure 13(e) and Figure 13(d), and Figure 13(j) is the logic difference image block between Figure 13(f) and Figure 13(d). It is undemanding to survey the difference between Figure 13(i) and Figure 13(j). Figure 13(i) and Figure 13(j) unmask that the reconstruction image quality of CDLPR outperforms that of DLPR. Figure 13 unmarks that the proposed method is effective for out-of-sample testing images with dark backgrounds and detailed foregrounds.

Figure 14 provides the experimental results of out-of-sample testing image 2. Figure 14 holds identical layout as Figure 13. It is stiff to inquiry the discrepancy between Figure 14(b) and Figure 14(c); It is also stiff to inquiry the discrepancy between Figure 14(e) and Figure 14(f); It is still stiff to inquiry the discrepancy between Figure 14(g) and Figure 14(h); It is simple to inquiry the discrepancy between Figure 14(i) and Figure 14(j). Figure 14(i) and Figure 14(j) state that the restoration image quality of CDLPR outbalances that of DLPR. Figure 14 states that the proposed method is propitious to out-of-sample testing images with dark backgrounds and delicate foregrounds.

Figure 15 affords the experimental results of out-of-sample testing image 3. Figure 15 holds identical composition as Figure 13. It is burdensome to investigate

the discrimination between Figure 15(b) and Figure 15(c); It is also burdensome to investigate the discrimination between Figure 15(e) and Figure 15(f); It is still burdensome to investigate the discrimination between Figure 15(g) and Figure 15(h); It is straightforward to investigate the discrimination between Figure 15(i) and Figure 15(j). Figure 15(i) and Figure 15(j) declare that the recovery image quality of CDLPR overmatches that of DLPR. Figure 15 declares that the proposed method is appropriate for out-of-sample testing images with dark backgrounds and exquisite foregrounds.

Figure 16 furnishes the experimental results of out-of-sample testing image 4. Figure 16 holds identical arrangement as Figure 13. It is rough to research the distinction between Figure 16(b) and Figure 16(c); It is also rough to research the distinction between Figure 16(e) and Figure 16(f); It is still rough to research the distinction between Figure 16(g) and Figure 16(h); It is explicit to research the distinction between Figure 16(i) and Figure 16(j). Figure 16(i) and Figure 16(j) express that the reestablishment image quality of CDLPR exceeds that of DLPR. Figure 16 expresses that the proposed method is fit for out-of-sample testing images with dark backgrounds and intricate patterns.

Figure 17 supplies the experimental results of out-of-sample testing image 5. Figure 17 holds identical organization as Figure 13. It is onerous to look up the distinguishing between Figure 17(b) and Figure 17(c); It is also onerous to look up the distinguishing between Figure 17(e) and Figure 17(f); It is still onerous to look up the distinguishing between Figure 17(g) and Figure 17(h); It is unambiguous to look up the distinguishing between Figure 17(i) and Figure 17(j). Figure 17(i) and Figure 17(j) present that the rebuilding image quality of CDLPR surpasses that of DLPR. Figure 17 presents the proposed method is suitable for out-of-sample testing images with high contrast and tangled patterns.

All in all, the proposed CIC is superior to the classical SIC in reconstruction performance and is especially suitable for out-of-sample testing images with dark backgrounds, detailed foregrounds, complicated patterns, and high contrast.

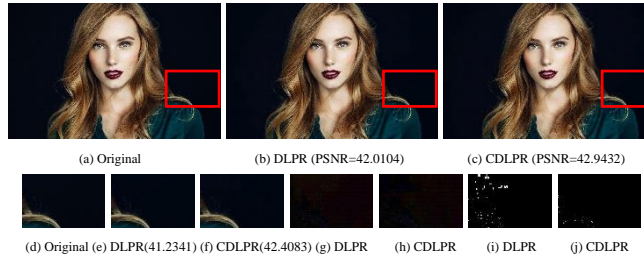


Fig. 13. Experimental results of DLPR and CDLPR for out-of-sample testing image 1.



Fig. 14. Experimental results of DLPR and CDLPR for out-of-sample testing image 2.

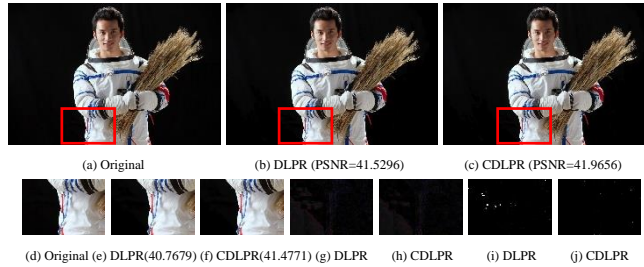


Fig. 15. Experimental results of DLPR and CDLPR for out-of-sample testing image 3.

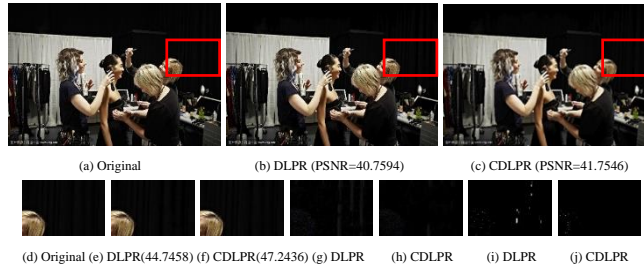


Fig. 16. Experimental results of DLPR and CDLPR for out-of-sample testing image 4.

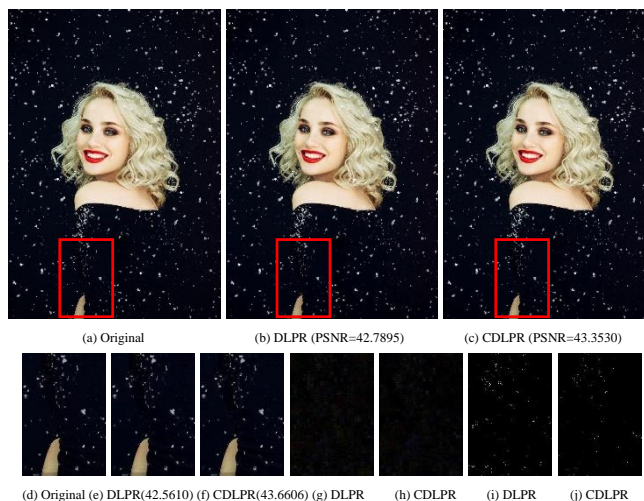


Fig. 17. Experimental results of DLPR and CDLPR for out-of-sample testing image 5.

V. CONCLUSION

This paper proposes the CIC framework which is a mixture of open-loop and closed-loop architectures. The open-loop structure comprises encoding and decoding units while the closed-loop structure comprises coding element, decoding element, summator, multiplier, and integrator. The proposed CIC is described by a nonlinear loop equation which is resolved by linear approximation of Taylor series expansion, and the zero steady-state error of the proposed CIC is mathematically proved. The proposed CIC can minimize the intrinsic difference between testing and training images and improve the performance of image reconstruction. The proposed CIC holds the property of plug-and-play and Post-Training and can be established on any existing advanced SIC algorithms. The experimental results on five public image compression datasets show that the proposed CIC outperforms five open-source state-of-the-art SIC approaches. Experimental results further show that the proposed CIC is particularly effective for out-of-sample testing images with dark backgrounds, sharp edges, high contrast, grid shapes, and complex patterns.

In our future work, the proposed CIC will be verified on more public image compression datasets and more leading open-source SIC methods. The proposed CIC will also be incorporated into In-Training procedure. Some advanced control theory, such as fuzzy logic, will further be considered in the proposed CIC.

AUTHOR CONTRIBUTIONS

Conceptualization, Honggui LI and Maria TROCAN; Methodology, Honggui LI and Dimitri GALAYKO; Writing, Honggui LI and Sinan CHEN; Experiment, Honggui LI and Nahid MD LOKMAN HOSSAIN; Supervision, Mohamad SAWAN. All authors have read and agreed to the published version of the manuscript.

COMPETING INTERESTS

The authors declare that they have no known competing financial interests or personal relationships that could have appeared to influence the work reported in this paper.

ACKNOWLEDGMENT

The authors would very much like to thank all the authors of the competing algorithms for selflessly releasing their source codes of image compression on the Microsoft GitHub website. The open-source codes allow us to easily implement the proposed algorithm depending on the competing algorithms. The authors also would very much like to express deep thanks to Google COLAB for its free GPU computing service.

REFERENCES

- [1] S. Noy and W. Zhang, "Experimental evidence on the productivity effects of generative artificial intelligence," *Science*, vol. 381, no. 6654, pp. 187-192, Jul. 2023, doi: 10.1126/science.adh2586.
- [2] S. Jamil, M. J. Piran, M. Rahman, and O.J. Kwon, "Learning-driven lossy image compression: A comprehensive survey," *Eng. Appl. Artif. Intell.*, vol. 123, no. B, Art. no. 106361, Aug. 2023, doi: 10.1016/j.engappai.2023.106361.
- [3] C. H. Huang and J. L. Wu, "Unveiling the future of human and machine coding: A survey of end-to-end learned image compression," *Entropy*, vol. 26, no. 5, pp. 1-35, May 2024, doi: 10.3390/e26050357.
- [4] B. A. Lungisani, C. K. Lebekwe, A. M. Zungeru, and A. Yahya, "Image compression techniques in wireless sensor networks: A survey and comparison," *IEEE Access*, vol. 10, pp. 82511-82530, Aug. 2022, doi: 10.1109/ACCESS.2022.3195891.
- [5] D. Mishra, S. K. Singh, and R. K. Singh, "Deep architectures for image compression: A critical review," *Signal Process.*, vol. 191, Art. no. 108346, Feb. 2022, doi: 10.1016/j.sigpro.2021.108346.
- [6] J. Y. Li, P. G. Chen, S. Z. Yu, S. Liu, and J. Y. Jia, "MOODv2: Masked image modeling for out-of-distribution detection," *IEEE Trans. Pattern Anal. Mach. Intell.*, Early Access, Jun. 2024, doi: 10.1109/TPAMI.2024.3412004.
- [7] S. H. Li, W. R. Dai, Y. M. Fang, Z. Y. Zheng, W. Fei, H. K. Xiong, W. Zhang, "Revisiting learned image compression with statistical measurement of latent representations," *IEEE Trans. Circuits Syst. Video Technol.*, vol. 34, no. 4, pp. 2891-2907, Apr. 2024, doi: 10.1109/TCSVT.2023.3300316.
- [8] K. Tsubota and K. Aizawa, "Content-adaptive optimization framework for universal deep image compression," *IEICE Trans Inf. Syst.*, vol. E107, no. 2, pp. 201-211, Feb. 2024, doi: 10.1587/transinf.2023EDP7114.
- [9] J. M. Zhu, Y. Q. Yang, T. P. Zhang, and Z. Q. Cao, "Finite-time stability control of uncertain nonlinear systems with self-limiting control terms," *IEEE Trans Neur. Net. Lear. Syst.*, vol. 34, no. 11, pp. 9514-9519, Nov. 2023, doi: 10.1109/TNNLS.2022.3149894.
- [10] X. N. Xia, T. P. Zhang, G. P. Kang, and Y. Fang, "Adaptive control of uncertain nonlinear systems with discontinuous input and time-varying input delay," *IEEE Trans Syst. Man Cyber.-Syst.*, vol. 52, no. 11, pp. 7248-7258, Nov. 2022, doi: 10.1109/TSMC.2022.3158617.
- [11] H. Li, N. M. L. Hossain, M. Trocan, M. Sawan, D. Galayko, "CMISR: circular medical image super-resolution," *Eng. Appl. Artif. Intell.*, vol. 33, no. B, Art. no. 108222, Jul. 2024, doi: 10.1016/j.engappai.2024.108222.
- [12] H. Li, M. Trocan, D. Galayko, M. Sawan, "ICRICS: iterative compensation recovery for image compressive sensing," *Signal, Image and Video Processing*, vol. 17, no. 6, 2953-2969, Sep. 2023, doi: 10.1007/s11760-023-02516-z.
- [13] H. Li, M. Trocan, M. Sawan, D. Galayko, "CSwin2SR: circular Swin2SR for compressed image super-resolution," in *IEEE 5th Int. Conf. on Artificial Intelligence Circuits and Systems (AICAS2023)*, Hangzhou, Zhejiang, China, pp. 1-5.

- [14]P. X. Wei, Z. W. Xie, G. B. Li, and L. Lin, "Taylor neural network for real-world image super-resolution," *IEEE Trans. Image Process.*, vol. 32, pp. 1942-1951, Apr. 2023, doi: 10.1109/TIP.2023.3255107.
- [15]Y. E. Bao, W. Tan, L. F. Zheng, F. Y. Meng, W. Liu, and Y. S. Liang, "Taylor series based dual-branch transformation for learned image compression," *Signal Process.*, vol. 212, Art. no. 109128, Nov. 2023, doi: 10.1016/j.sigpro.2023.109128.
- [16]A. Ebner and M. Haltmeier, "Plug-and-play image reconstruction is a convergent regularization method," *IEEE Trans. Image Process.*, vol. 33, pp. 1476-1486, Mar. 2024, doi: 10.1109/TIP.2024.3361218.
- [17]Y. Chen, X. F. Gui, J. S. Zeng, X. L. Zhao, and W. He, "Combining low-rank and deep plug-and-play priors for snapshot compressive imaging," *IEEE Trans. Neur. Net. Lear. Syst.*, Early Access, Jul. 2023, doi: 10.1109/TNNLS.2023.3294262.
- [18]T. T. Wu, W. N. Wu, Y. Yang, F. L. Fan, and T. Y. Zeng, "Retinex image enhancement based on sequential decomposition with a plug-and-play framework," *IEEE Trans. Neur. Net. Lear. Syst.*, Early Access, Jun. 2023, doi: 10.1109/TNNLS.2023.3280037.
- [19]U. S. Kamilov, C. A. Bouman, G. T. Buzzard, and B. Wohlberg, "Plug-and-play methods for integrating physical and learned models in computational imaging: theory, algorithms, and applications," *IEEE Signal Process. Mag.*, vol. 40, no. 1, pp. 85-97, Jan. 2023, doi: 10.1109/MSP.2022.3199595.
- [20]K. Zhang, Y. W. Li, W. M. Zuo, L. Zhang, G. L. Van, and R. Timofte, "Plug-and-play image restoration with deep denoiser prior," *IEEE Trans. Pattern Anal. Mach. Intell.*, vol. 44, no. 10, pp. 6360-6376, Nov. 2021, doi: 10.1109/TPAMI.2021.3088914.
- [21]S. M. Zandavi, "Post-trained convolution networks for single image super-resolution," *Artif. Intell.*, vol. 318, Art. no. 103882, May 2023, doi: 10.1016/j.artint.2023.103882.
- [22]Y. C. Bai, X. M. Liu, K. Wang, X. Y. Ji, X. L. Wu, and W. Gao, "Deep lossy plus residual coding for lossless and near-lossless image compression," *IEEE Trans. Pattern Anal. Mach. Intell.*, vol. 46, no. 5, pp. 3577-3594, May 2024, doi: 10.1109/TPAMI.2023.3348486.
- [23]R. H. Yang and S. Mandt, "Lossy image compression with conditional diffusion models," in the 37th Conf. on Neural Information Processing Systems, New Orleans, LA, USA, 2023, pp. 1-25.
- [24]Y. C. Bai, X. Yang, X. M. Liu, J. J. Jiang, Y. W. Wang, X. Y. Ji, and W. Gao, "Towards end-to-end image compression and analysis with transformers," in the 36th AAAI Conf. on Artificial Intelligence, Virtual, Online, 2022, pp. 104-112.
- [25]Z. B. Zhang, S. Esenlik, Y. J. Wu, M. Wang, K. Zhang, and L. Zhang, "End-to-end learning-based image compression with a decoupled framework," *IEEE Trans. Circuits Syst. Video Technol.*, vol. 34, no. 5, pp. 3067-3081, May 2024, doi: 10.1109/TCSVT.2023.3313974.
- [26]D. Y. Zhang, F. Li, M. Liu, R. M. Cong, H. H. Bai, M. Wang, and Y. Zhao, "Exploring resolution fields for scalable image compression with uncertainty guidance," *IEEE Trans. Circuits Syst. Video Technol.*, vol. 34, no. 4, pp. 2934-2948, Apr. 2024, doi: 10.1109/TCSVT.2023.3307438.
- [27]N. D. Jr Guerin, R. C. da Silva, B. Macchiavello, "Learning-based image compression with parameter-adaptive rate-constrained loss," *IEEE Signal Process. Lett.*, 31, 1099-1103, Apr. 2024, doi: 10.1109/LSP.2024.3383801.
- [28]W. C. Zhang, Y. J. Liu, L. Y. Chen, J. H. Shi, X. M. Hong, and X. B. Wang, "Semantically-disentangled progressive image compression for deep space communications: Exploring the ultra-low rate regime," *IEEE J. Sel. Area Comm.*, vol. 42, no. 5, pp. 1130-1144, May 2024, doi: 10.1109/JSAC.2024.3369654.
- [29]H. S. Fu, F. Liang, J. P. Lin, B. Li, M. Akbari, J. Liang, G. H. Zhang, D. Liu, C. J. Tu, and J. N. Han, "Learned image compression with Gaussian-Laplacian-logistic mixture model and concatenated residual modules," *IEEE Trans. Image Process.*, vol. 32, pp. 2063-2076, May 2023, doi: 10.1109/TIP.2023.3263099.
- [30]Z. H. Duan, M. Lu, Z. Ma, and F. Q. Zhu, "Lossy image compression with quantized hierarchical VAEs," in the IEEE Winter Conf. on Applications of Computer Vision, Waikoloa, HI, USA, pp. 198-207.
- [31]A. Timur, "Vector quantized variational image compression," Skolkovo Institute of Science and Technology, Moscow, Russia, Tech. Rep. of Bayesian Methods of Machine Learning, Sep. 2022.
- [32]S. L. Cai, L. Q. Chen, Z. J. Zhang, X. Y. Zhao, J. H. Zhou, Y. X. Peng, L. X. Yan, S. Zhong, and X. Zou, "I2C: Invertible continuous codec for high-fidelity variable-rate image compression," *IEEE Trans. Pattern Anal. Mach. Intell.*, vol. 46, no. 6, pp. 4262-4279, Jun. 2024, doi: 10.1109/TPAMI.2024.3356557.

- [33]H. S. Fu, F. Liang, J. Liang, B. L. Li, G. H. Zhang, and J. N. Han, "Asymmetric learned image compression with multi-scale residual block, importance scaling, and post-quantization filtering," *IEEE Trans. Circuits Syst. Video Technol.*, vol. 33, no. 8, pp. 4309-4321, Aug. 2023, doi: 10.1109/TCSVT.2023.3237274.
- [34]G. Zhang, X. F. Zhang, and L. Tang, "Enhanced quantified local implicit neural representation for image compression," *IEEE Signal Process. Lett.*, vol. 30, pp. 1742-1746, Mar. 2023, doi: 10.1109/LSP.2023.3334956.
- [35]J. Y. Guo, D. Xu, and G. Lu, "CBANet: Toward complexity and bitrate adaptive deep image compression using a single network," *IEEE Trans. Image Process.*, vol. 32, pp. 2049-2062, May 2023, doi: 10.1109/TIP.2023.3251020.
- [36]Z. Y. Jiang, X. H. Liu, A. N. Li, and G. Y. Wang, "Enhancing high-resolution image compression through local-global joint attention mechanism," *IEEE Signal Process. Lett.*, vol. 31, pp. 1044-1048, Jun. 2024, doi: 10.1109/LSP.2024.3383963.
- [37]B. Li, Y. J. Li, J. C. Luo, X. R. Zhang, C. Y. Li, Z. M. Chenjin, and Y. Liang, "Learned image compression via neighborhood-based attention optimization and context modeling with multi-scale guiding," *Eng. Appl. Artif. Intell.*, vol. 129, Mar. 2024, Art. no. 107596, doi: 10.1016/j.engappai.2023.107596.
- [38]Z. S. Tang, H. L. Wang, X. K. Yi, Y. Zhang, S. Kwong, and C. C. J. Kuo, "Joint graph attention and asymmetric convolutional neural network for deep image compression," *IEEE Trans. Circuits Syst. Video Technol.*, vol. 33, no. 1, pp. 421-433, Jan. 2023, doi: 10.1109/TCSVT.2022.3199472.
- [39]J. Q. Shi, M. Lu, and Z. Ma, "Rate-distortion optimized post-training quantization for learned image compression," *IEEE Trans. Circuits Syst. Video Technol.*, vol. 34 no. 5, pp. 3082-3095, May 2024, doi: 10.1109/TCSVT.2023.3323015.
- [40]Z. H. Duan, M. Lu, J. Ma, Y. N. Huang, Z. Ma, and F. Q. Zhu, "QARV: Quantization-aware ResNet VAE for lossy image compression," *IEEE Trans. Pattern Anal. Mach. Intell.*, vol. 46, no. 1, pp. 436-450, Jan. 2024, doi: 10.1109/TPAMI.2023.3322904.
- [41]S. H. Li, H. Li, W. R. Dai, C. L. Li, J. N. Zou, and H. K. Xiong, "Learned progressive image compression with dead-zone quantizers," *IEEE Trans. Circuits Syst. Video Technol.*, vol. 33, no. 6, pp. 2962-2978, Jun. 2023, doi: 10.1109/TCSVT.2022.3229701.
- [42]H. Son, T. Kim, H. Lee, and S. Lee, "Enhanced standard compatible image compression framework based on auxiliary codec networks," *IEEE Trans. Image Process.*, vol. 31, pp. 664-677, Jan. 2022, doi: 10.1109/TIP.2021.3134473.
- [43]J. F. Li, X. Y. Liu, Y. Q. Gao, L. Zhuo, and J. Zhang, "BARRN: A blind image compression artifact reduction network for industrial IoT systems," *IEEE Trans Ind. Inform.*, vol. 19, no. 9, pp. 9479-9490, Sep. 2023, doi: 10.1109/TH.2022.3228777.
- [44]L. Ma, Y. F. Zhao, P. X. Peng, and Y. H. Tian, "Sensitivity decouple learning for image compression artifacts reduction," *IEEE Trans. Image Process.*, vol. 33, pp. 3620-3633, Jun. 2024, doi: 10.1109/TIP.2024.3403034.
- [45]J. H. Hu, G. X. Luo, B. Wang, W. M. Wu, J. H. Yang, and J. D. Guo, "Residual network for image compression artifact reduction," *Int. J. Pattern Recogn. Artif. Intell.*, vol. 38, no. 2, Mar. 2024, Art. no. 2454001, doi: 10.1142/S0218001424540016.
- [46]H. G. Chen, X. H. He, H. Yang, L. B. Qing, and Q. Z. Teng, "A feature-enriched deep convolutional neural network for JPEG image compression artifacts reduction and its applications," *IEEE Trans. Neur. Net. Lear. Syst.*, vol. 33, no. 1, pp. 430-444, Jan. 2022, doi: 10.1109/TNNLS.2021.3124370.

BIOGRAPHIES



learning, computer vision, and embedded computing.

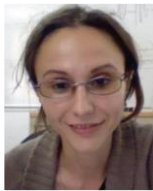
Honggui LI received a B.S. degree in electronic science and technology from Yangzhou University and received a Ph.D. degree in mechatronic engineering from Nanjing University of Science and Technology. He is a senior member of the Chinese Institute of Electronics. He is a visiting scholar and a post-doctoral fellow at Institut Supérieur d'Électronique de Paris for one year. He is an associate professor of electronic science and technology and a postgraduate supervisor of electronic science and technology at Yangzhou University. He is a reviewer for some international journals and conferences. He is the author of over 30 refereed journal and conference articles. His current research interests include machine learning, deep



Sinan CHEN received a B.E. degree in electronics information engineering from Yangzhou University in China. He is now studying for a master's degree in integrated circuits engineering at Yangzhou University in China.



Nahid MD LOKMAN HOSSAIN received a B.S. degree in computer science and technology from Chongqing University of Posts and Telecommunications in China. He is now studying for a master's degree in software engineering at Yangzhou University in China. His research interests include machine learning, computer vision, innovation software, cloud computing, and big data.



Maria TROCAN received a M.Eng. in Electrical Engineering and Computer Science from the Politehnica University of Bucharest, a Ph.D. in Signal and Image Processing from Telecom ParisTech, and the Habilitation to Lead Researches (HDR) from Pierre & Marie Curie University (Paris 6). She has joined Joost - Netherlands, where she worked as a research engineer involved in the design and development of video transcoding systems. She is firstly Associate Professor, then Professor at Institut Supérieur d'Electronique de Paris (ISEP). She is an Associate Editor for the Springer Journal on Signal, Image and Video Processing and a Guest Editor for several journals (Analog Integrated Circuits and Signal Processing, IEEE Communications Magazine, etc.). She is an active member of IEEE France and served as a counselor for the ISEP IEEE Student Branch, IEEE France Vice-President responsible for Student Activities, and IEEE Circuits and Systems Board of Governors member, as Young Professionals representative. Her current research interests focus on image and video analysis & compression, sparse signal representations, machine learning, and fuzzy inference.



Dimitri GALAYKO received a bachelor's degree from Odessa State Polytechnic University in Ukraine, a master's degree from the Institute of Applied Sciences of Lyon in France, and a Ph.D. degree from University of Lille in France. He made his Ph.D. thesis at the Institute of Microelectronics and Nanotechnologies. His Ph.D. dissertation was on the design of micro-electromechanical silicon filters and resonators for radio communications. He is a Professor at the LIP6 research laboratory of Sorbonne University in France. His research interests include the study, modeling, and design of nonlinear integrated circuits for sensor interfaces and mixed-signal applications. His research interests also include machine learning and fuzzy computing.



Mohamad SAWAN received a Ph.D. degree in electrical engineering from the University of Sherbrooke, Sherbrooke, QC, Canada, in 1990. He was a Chair Professor awarded with the Canada Research Chair in Smart Medical Devices (2001–2015) and was leading the Microsystems Strategic Alliance of Quebec - ReSMiQ (1999–2018). He is a Professor of Microelectronics and Biomedical Engineering, in leave of absence from Polytechnique Montréal, Canada. He joined Westlake University, Hangzhou, China, in January 2019, where he is a Chair Professor, Founder, and Director of the Center for Biomedical Research And Innovation (CenBRAIN). He has published more than 800 peer-reviewed articles, two books, ten book chapters, and 12 patents. He founded and chaired the IEEE-Solid State Circuits Society Montreal Chapter (1999–2018) and founded the Polystim Neurotech Laboratory, Polytechnique Montréal (1994–present), including two major research infrastructures intended to build advanced Medical devices. He is the Founder of the International IEEE-NEWCAS Conference, and the Co-Founder of the International IEEE-BioCAS, ICECS, and LSC conferences. He is a Fellow of the Royal Society of Canada, a Fellow of the Canadian Academy of Engineering, and a Fellow of the Engineering Institutes of Canada. He is also the "Officer" of the National Order of Quebec. He has served as a member of the Board of Governors (2014–2018). He is the Vice-President of Publications (2019–present) of the IEEE CAS Society. He received several awards, among them the Queen Elizabeth II Golden Jubilee Medal, the Barbara Turnbull 2003 Award for spinal cord research, the Bombardier and Jacques-Rousseau Awards for academic

achievements, the Shanghai International Collaboration Award, and the Medal of Merit from the President of Lebanon for his outstanding contributions. He was the Deputy Editor-in-Chief of the IEEE TRANSACTIONS ON CIRCUITS AND SYSTEMS-II: EXPRESS BRIEFS (2010–2013); the Co-Founder, an Associate Editor, and the Editor-in-Chief of the IEEE TRANSACTIONS ON BIOMEDICAL CIRCUITS AND SYSTEMS; an Associate Editor of the IEEE TRANSACTIONS ON BIOMEDICALS ENGINEERING; and the International Journal of Circuit Theory and Applications.